PAPER

Stray field and combined effects on device miniaturization of the magnetic tunnel junctions

View the article online for updates and enhancements.

You may also like

Stray field and combined effects on device miniaturization of the magnetic tunnel junctions

Chih-Wei Cheng[1]**, Kuan-Ming Chen**[1]**, Jeng-Hua Wei**[2]**, Yu-Chen Hsin**[2]**, Shyh-Shyuan Sheu**[2]**, Chih-I Wu**[2,3] **and Yuan-Chieh Tseng**[1,*]

[1] Department of Materials Science and Engineering, National Yang Ming Chiao Tung University, Hsinchu, Taiwan
[2] Electronic and Optoelectronic System Research Laboratories, Industrial Technology Research Institute (ITRI), Hsinchu, Taiwan
[3] Department of Physics, National Taiwan University, Taipei, Taiwan

E-mail: yctseng1978@nycu.edu.tw

Abstract

Magneto-static stray field (H_{stray}) interactions become an important issue when perpendicular CoFeB/MgO magnetic tunnel junctions (MTJs) are miniaturized. This raises the issue of which of the two mainstream etching processes, the pillar structure and the step structure, is better able to retain MTJ performance at extremely small scales. In the current study, we first simulated H_{stray} effects as a function of Ruderman–Kittel–Kasuya–Yosida strength within a synthetic antiferromagnetic structure for the two structures. Our results revealed that H_{stray} interactions were less influential (in terms of offset field) in step MTJs than in pillar MTJs during MTJ miniaturization. This is in good agreement with experimental results. This finding is further supported by adding Dzyaloshinskii–Moriya interactions into the free-layer of the two structures. We further simulated thermal stability with the inclusion of H_{stray} for 30 nm MTJs. We found that adding etching damage effects (i.e. assuming both anisotropy constant and saturation magnetization of the free layer had some degree of loss) into the model of the pillar MTJ was necessary to obtain a trend that is close to the experimental results of thermal stability. This information can provide some guidance on the technical choices for the MTJ miniaturization.

Supplementary material for this article is available online

Keywords: spin-transfer torque, Dzyaloshinskii–Moriya interactions, magnetic tunnel junction, stray field, micromagnetic simulation, sidewall etching damage

(Some figures may appear in colour only in the online journal)

1. Introduction

Spin-transfer torque magneto-resistive random access memory (STT-MRAM) has become a favorable candidate for the next generation of embedded memory applications due

to its fast read/write speed, long cyclic durability, and compatibility with metal oxide semiconductor processes [1–3]. The basic element of STT-MRAM is a magnetic tunnel junction (MTJ). Modern technology trends suggest that MTJs must be scaled down to 30 nm or smaller without affecting their thermal stability [4]. So far, one of the obstacles to commercializing STT-MRAM is the sidewall damage that occurs during the etching process, which is a severe

---

* Author to whom any correspondence should be addressed.

issue affecting the precision of component scaling. Non-volatility of the stored information in CoFeB/MgO/CoFeB MTJs requires equal thermal stability between the two remanent states of the free layer (FL). Unfortunately, magneto-static stray field (H_{stray}) effects in perpendicular MTJs (pMTJs) increase inversely with the dimensions of the MTJ [5, 6]. H_{stray} effects can introduce serious read errors by making one reversal more favorable than the other. Pillar [3, 7] structures have been widely adopted to increase the density of MTJs, and step [8–11] structures have been used to simplify fabrication. At this point, however, it is unclear which structure is less prone to H_{stray} effects under MTJ miniaturization. As shown in figure 1, the H_{stray} generated in the reference layer (RL) tends to stabilize the parallel (P) state, while destabilizing the antiparallel (AP) state of the FL [11–13]. This can produce an offset in the M-H loop of the MTJ, henceforth denoted as H_{off}. Ideally, H_{stray} can be mitigated using a synthetic antiferromagnet (SAF) structure [5, 8, 14, 15], in which the RL and hard layer (HL) enable magnetic-flux closure via antiferromagnetic coupling. Theoretically, this should minimize H_{stray} from the RL; however, in practice, the effectiveness of the SAF structures is limited. This can be attributed to the fact that the FL itself has an H_{stray}, which interacts with the H_{stray} from the SAF in a complex manner, resulting in the H_{off} observed in the M-H loop. This means that it is not possible to estimate H_{stray} effects from the SAF alone based on experiment results.

The evaluation of device-level magnetic components in experiments is generally performed by measuring the hysteresis in electrical resistivity and the magnetic field (RH). However, the quality of the measurement results is determined by extrinsic parameters (etching process and electrical measurement technologies) and extremely dependent on magnetization reversal mechanisms. This makes it difficult to directly and objectively observe the influence of process conditions on the properties of the component. In this work, we used an object-oriented micro-magnetic framework (OOMMF) [16] to simulate pure SAF H_{stray} effects without considering the H_{stray} effects of the FL under pillar and step MTJ miniaturization. We then incorporated the H_{stray} effects of the FL into the model to generate H_{off}, and compared it with experiment results. In order to be closer to the real situation, we added the etching damage effects to the theoretical model. Finally, we added Dzyaloshinskii–Moriya interactions (DMI) [17–21] to further enrich the model. We also performed micromagnetic simulation with string method to determine the minimum energy path and saddle point (i.e. switching transition point) to estimate the thermal stability factor (Δ) for the two structures with different MTJ sizes. We also considered the etching effects in Δ. We believe that this will give a more comprehensive view of MTJ's miniaturization effect.

2. Experiment and simulation

Our focus in this study was on the pillar and step MTJs currently under development for STT-MRAM devices. The stacking configurations of the two MTJs are illustrated in figure 1. Same stackings were used for simulations and experiments

(i.e. offset field measurements). We adopted a $(Co/Pt)_n$ bilayer in the design of the RL and HL (varying repetition number *n*) with Ru as a spacer layer. RL, Ru, and HL were the constituents of the SAF layer. Note that the thicknesses of RL and Ru remained fixed, while the thickness of the HL was varied with the aim of manipulating Ruderman–Kittel–Kasuya–Yosida (RKKY) interactions to generate different H_{stray} output values. We also employed a CoFeB spin-polarizing layer (SPL). Supplementary table I (available online at stacks.iop.org/JPhysD/55/195002/mmedia) lists the calculation parameters for each layer. Gilbert damping in the FL was set at 0.01. In our analysis of scaling, the diameter of the MTJ was varied between 20 and 100 nm from the MgO to the bottom. We then calculated the SAF-generated H_{stray} on the surface of the MgO in the horizontal (*x*) and vertical (*y*) directions. Calculations were conducted at zero K to eliminate thermal fluctuations. Because we found in calculation that the magnetic properties of the MTJs were less affected by the size when the SAF exceeded 100 nm (see supplementary SF-1), we focus our calculation on the MTJ size not exceeding 100 nm. In experiments, pMTJs based on the stacking configuration (figure 1) were deposited via magnetron sputtering on a thermally-oxidized Si substrate at room temperature and then annealed at 300 °C for 2 h. E-beam lithography was used to pattern the pMTJ into pillar and step structures (etching endpoint at the MgO barrier), with diameters of 30, 80, 130, and 180 nm.

The experimental thermal stability factors of 30 nm pillar and step MTJs were extracted from switching field distribution measurements following a simple thermal activation model [11, 15, 22]. The switching probability was fitted based on the equation:

$$\text{CDF}(\%) = 100 \times \left\{ 1 - \exp \left[\frac{-H_k f_0 \sqrt{\pi}}{2R\sqrt{\Delta}} \times \text{erfc} \left(\sqrt{\Delta} \times \left(1 - \frac{H - H_{applied}}{H_k} \right) \right) \right] \right\} \quad (1)$$

where f_0 is the attempt frequency ($\approx$1 GHz), R is the field sweeping rate (50 Oe/s), H_k is the anisotropy field, Δ is the thermal stability factor and $H_{applied}$ is the applied field to compensate H_{stray}. Δ values of the 30 nm pillar and step MTJs (figure 7) were obtained from fitting the switching probability functions of 100 magneto-resistance (defined as R-H henceforth) loops of the two structures.

3. Results and discussion

The stacking configurations of the pillar and step MTJs are illustrated in figures 1(a) and (b), respectively. Note that we used the same stacking parameters for simulations and experiments (offset field, figure 5). The cross-sectional TEM image of the pillar and step MTJs are shown in figures 1(c) and (d), respectively. The TEM data show that in the pillar MTJ, the film structure above the MgO is almost as wide as the MgO itself (the difference is due to the imperfection of the etching process), but in the step MTJ, the MgO is much wider than the
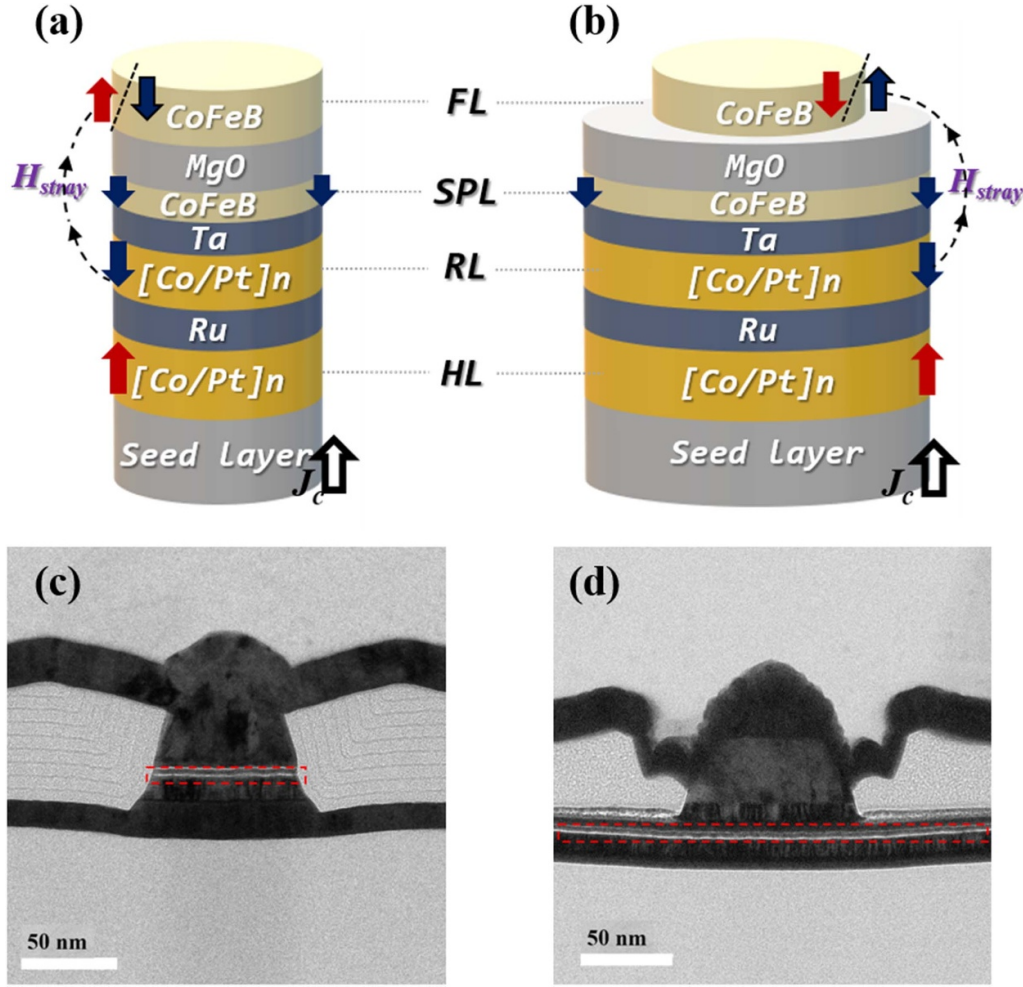
J. Phys. D: Appl. Phys. **55** (2022) 195002

C-W Cheng *et al*

Figure 1. MTJ stacks used in (a) pillar and (b) step structures with AP/P states where vertical arrows represent alignment direction of magnetic moment in each layer and FL, SPL, RL, and HL respectively refer to free, spin-polarizing, reference, and hard layers. TEM cross-sectional images of (c) pillar and (d) step MTJs. Red dashed boxes highlight the MgO stack in the two MTJs.

top layers. Note that because the MTJ structure is too complicated, we had to select the key differences between the two MTJs in terms of structure for calculation. It has been reported that the etching process will likely cause redeposition of the sputtered atoms onto the MTJ sidewall, and this consequently results in the increase of the MTJ size or barrier short [12]. This is a serious problem for the pillar MTJs. On the contrary, the step structure could avoid this problem by etching stopped at the MgO layer. We thus used micromagnetic simulation to test the changes of switching-time and Δ of the pillar MTJs with different percentages of impaired anisotropy energy (K_u) and saturation magnetization (M_s), within a fixed sidewall damaged thickness of the 2 nm CoFeB FL. The detail of the result is presented in supplementary information SF-2.

Figure 2(a) illustrates the SAF-generated H_{stray} distribution on the MgO surface along the x- and z-directions as a function of MTJ size. The thickness of the HL was 2 nm. Changes in H_{stray} were tracked in various positions of the FL with H_{stray} sensing points maintained at a vertical distance of 0.75 nm from the top surface of the MgO. H_{stray} was weak in the center of the junction, growing in intensity toward the edges in

both the x- and z-directions. This can be attributed to the fact that the need for magnetic flux closure in H_{stray} increased sharply toward the edges. When the FL position changed from $+x$ to $-x$, H_{stray} switched signs to enable flux closure; however, H_{stray} remained close to zero in the center of the FL, irrespective of MTJ size. H_{stray} remained negative along the z-axis, increasing in the center of the FL inversely with the size of the MTJ. Figure 2(b) presents a top-view image showing H_{stray} contours along x-/z-directions (20 and 100 nm) supporting the conclusion above. These results indicate the following: (a) the FL experienced opposing H_{stray} effects, which were particularly pronounced along the edge of the MTJ in the horizontal (x) direction and (b) the center of the FL was subject to a significant increase in z-H_{stray} when the size of the MTJ decreased.

Figure 3(a) illustrates time-dependent AP $\rightarrow$ P and P $\rightarrow$ AP switching (lower figure) with the corresponding switching current density J_c (upper figure) in pillar and step MTJs. In simulations, the thicknesses of the HL and FL were respectively set at 2 and 20 nm in both structures. In the step MTJ, stacking beneath the FL was set at 80 nm. We added the STT terms
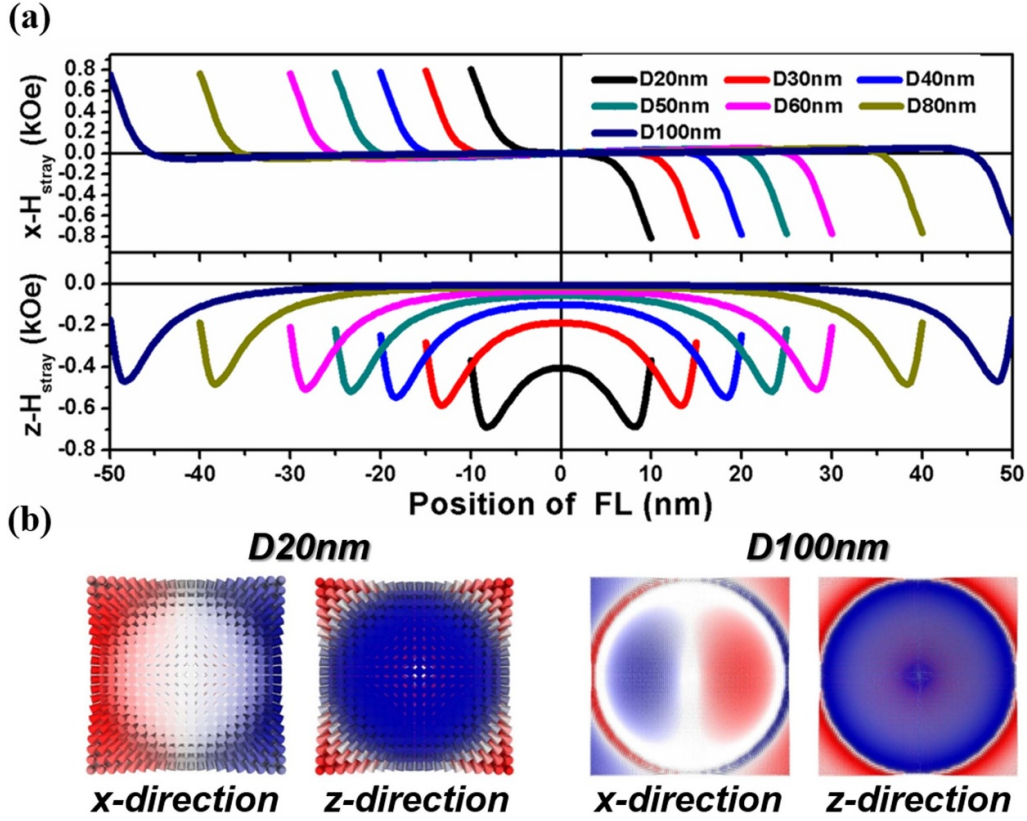
J. Phys. D: Appl. Phys. **55** (2022) 195002

C-W Cheng *et al*

Figure 2. (a) Calculated H$_{stray}$ distribution on MgO surface along *x*-direction (upper figure) and *z*-direction (lower figure) with MTJ diameters (20–100 nm) showing that H$_{stray}$ varied with location in FL; (b) H$_{stray}$ mapping contour along *x/z* directions in 20 nm (left) and 100 nm (right) MTJs.

in LLG equations in order to implement the STT module in OOMMF, as follows:

$$\frac{\partial \vec{m_s}}{\partial t} = -\gamma \vec{m_s} \times \vec{H}_{\text{eff}} + \alpha \vec{m_s} \times \frac{d\vec{m}}{dt} - \gamma a_J \vec{m_s} \times \left(\vec{m_s} \times \vec{m_p} \right)$$

(2)

where m_s, γ, H_{eff}, α, and m_p respectively refer to saturation magnetization, gyromagnetic ratio, effective field, damping constant, and direction of spin polarization. a_J is the STT coefficient proportional to spin current, where $a_J = \hbar P j / (2eMt)$ [20]. We found that AP → P required a J_c of only 0.8×10^{10} A m^{-2}; however, P → AP required a J_c of 1.6×10^{10} A m^{-2}. Moreover, the two structures took a similar amount of time to complete AP → P switching ($\triangle t \sim 1.3$ ns), whereas the pillar MTJ required far more time than did the step MTJ to complete P → AP switching ($\triangle t \sim 15$ ns). The spin configuration of the two MTJs changed during switching, as shown in the lower figures of figure 3. We can see that the switching mode involved domain wall (DW) motion [23–25]. As for simulation parameters, DW width $\lambda = 2\sqrt{A/K_{\text{eff}}}$ and critical diameter $d_c = (16/\pi)\sqrt{A/K_{\text{eff}}}$. The critical diameter is the maximum threshold below which thermally-activated switching is expected to be coherent [24, 25]. Our results ($\lambda = 6.3$ nm and $d_c = 16$ nm) revealed that in a 20 nm MTJ, DW motion dominated switching as characteristic of non-coherent rotation.

Figures 3(b) and (c) illustrate the distributions of SAF-produced H_{stray} on the surface of MgO along the *x*- and *z*-directions, in pillar and step MTJ, respectively. Note that in the pillar MTJs, H_{stray} distribution could be sensed only within ± 10 nm in the FL; however, in the step MTJ, H_{stray} distribution could be sensed over a width of ± 40 nm.

Under the same FL width (i.e. ± 10 nm), in-plane (*x*) and out-of-plane (*z*) H_{stray} effects were more suppressed in the step MTJ than in the pillar MTJ. This means that the SAF was more effective in the step MTJ than the pillar MTJ in reducing H_{stray}. In the pillar MTJ, we observed negative z-H_{stray} values even adjacent to the center of the FL, indicating that the initial state was subject to negative H_{stray} forces even when no current was applied. As shown in figure 3, when the initial state was AP, the corresponding negative H_{stray} facilitated AP → P switching. When the initial state was P-state, negative H_{stray} provided resistance against P → AP switching. Obviously, the pillar MTJ generates an intrinsic asymmetric z-H_{stray} effect, arising from RKKY interactions between the RL and HL. As shown in figure 4(a), we also monitored z-H_{stray} distribution while varying the thickness of the HL (2.0–4.0 nm) with the MTJ fixed at 20 nm. When the thickness of the HL was increased, z-H_{stray} increased due to a change in RKKY strength. Particularly in the center, we observed a gradual change in z-H_{stray} values from negative to positive. Figure 4(b) illustrates z-H_{stray} as a function of MTJ size (from 20 to 100 nm) with HL of various thicknesses. These results suggest that the effect of z-H_{stray} is
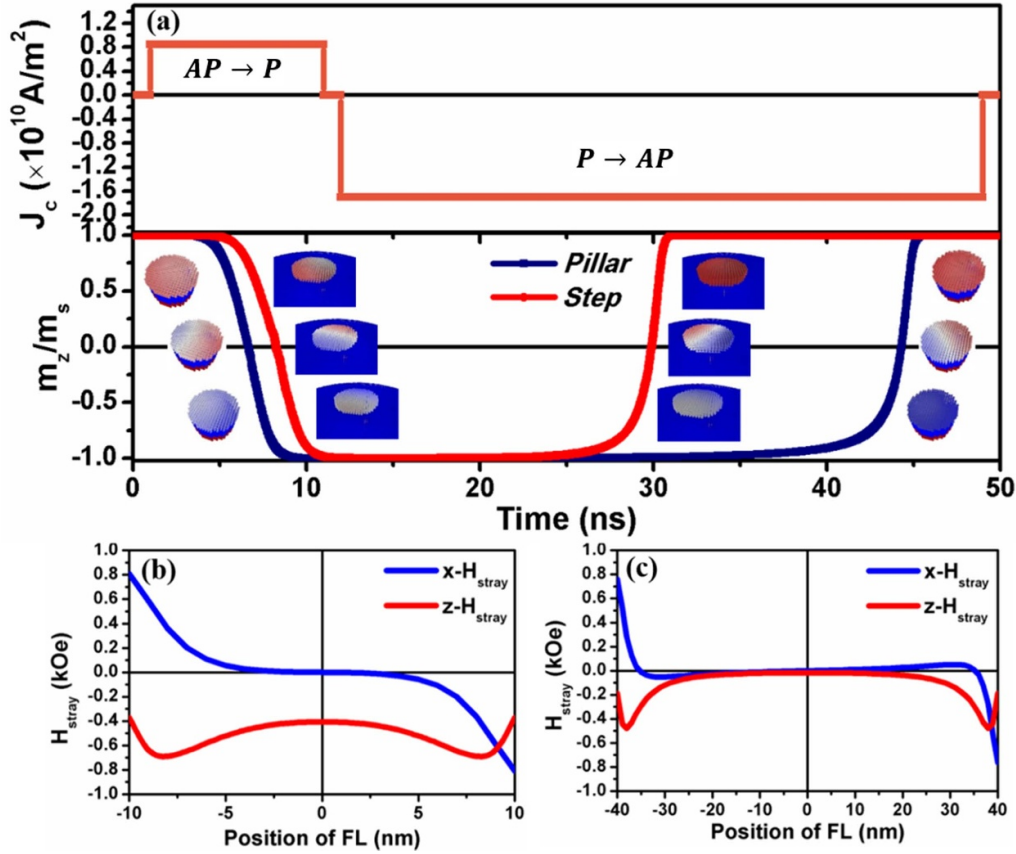
Figure 3. (a) switching current density in AP→P/P→AP switching with longer P→AP switching time for comparison to ensure switching completion in both structures. The reversal configurations of the two structures are shown as insets. In the analysis of switching, we used an FL layer (20 nm thick) with the initial magnetization direction tilted slightly (5 degrees) from perfectly perpendicular in order to reduce switching incubation time prior to the application of current (pulse width of 10 ns), followed by another relaxation interval; (b) and (c) present the $x(z)$-H$_{stray}$ distributions in various regions of FL for pillar and step MTJs, respectively.

insignificant in large MTJs and becomes more pronounced as the size of the MTJ is reduced. Furthermore, this phenomenon can be mitigated by increasing the thickness of the HL. As shown in supplementary SF-3, we simulated AP → P/P → AP switching probability as a function of current density in 20 nm pillar and step MTJs with HLs of various thicknesses. The pillar MTJ exhibited more variation in P → AP switching than in AP → P switching as a function of HL thickness. The step MTJ did not exhibit this behavior.

Figures 5(a) and (b) present normalized experimental R-H loops of the pillar and step MTJs, respectively. We obtained variable H_{off} with MTJ size in the pillar MTJs but this phenomenon was absent to the step MTJs. From the experiment, we observed that the step MTJ displayed better ability to resist H_{stray} effect than the pillar MTJ in terms of H_{off}. In figure 5(c), we added the parameters of the FL to the model in simulating H_{off} as a function of MTJ size in both structures. We then superimposed the experiment-derived H_{off} versus MTJ-size over the theoretical results. Overall, we observed good agreement between the two. In particular, when the sidewall damage effect (both K_u and M_s were degraded by 50% within a 2 nm thick area) was considered in the pillar MTJ, its H_{off} appeared closer to the experimental value while reducing the

MTJ size. This implies that the pillar MTJ does have some degree of sidewall damage.

Note that in theory, the two structures share the same H_{off} at 100 nm, due to the fact that this dimension was the first data point used in our calculations, such that there was no difference between the two. The H_{off} of the step MTJ decreased when MTJ size was reduced in simulations, but slightly increased in experiments. This can be attributed to the fact that in practice MTJs contain material imperfections capable of generating local variations in H_{stray}, hence leading to an increase in H$_{off}$. Overall, we determined that H_{off} in pillar MTJs gradually increased under the effects of MTJ shrinkage, due to high sensitivity to z-H$_{stray}$. By contrast, H_{off} in step MTJs remained stable under MTJ shrinkage.

We added the DMI to the FL to further verify our findings. The results are presented as H_{off} contour plots versus DMI strength (y-axis) and HL thickness (x-axis), in pillar MTJs of 20 (figure 6(a)), 30 (figure 6(b)), and 80 nm (figure 6(c)), and step MTJs of 20 nm (figure 6(d)). The Hamiltonian H_{DM} for interfacial DMI can be written as follows:
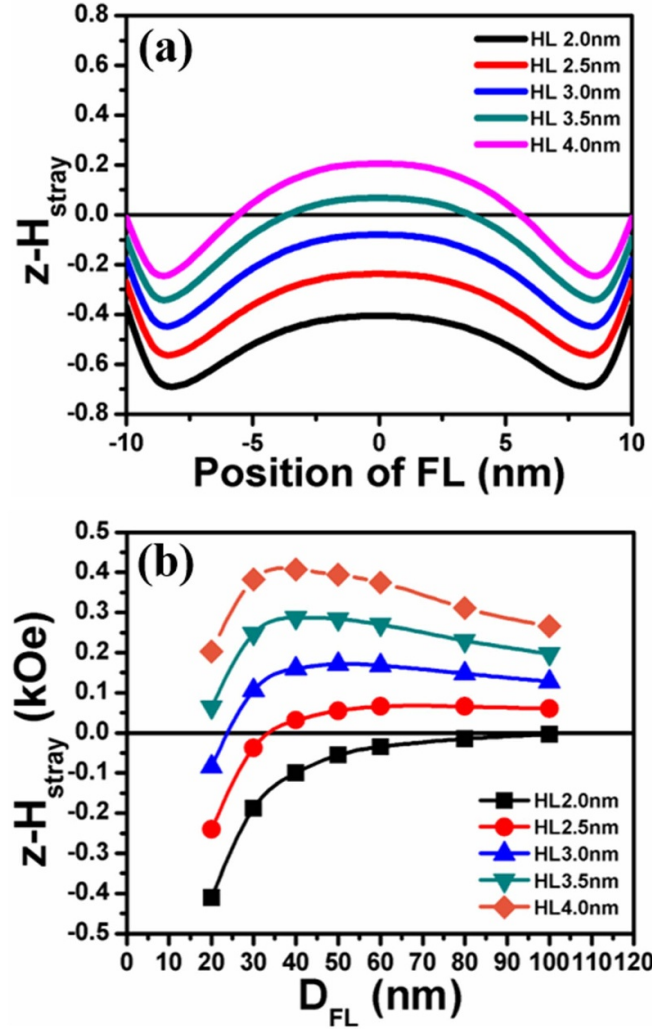
$$H_{DM} = -(S_1 \times S_2) \cdot D_{12} \tag{3}$$

Figure 4. (a) z-H_{stray} as a function of FL position with HLs of various thicknesses; (b) z-H_{stray} as a function of FL diameter with HLs of various thicknesses.

where S_1 and S_2 are neighboring spins, and D_{12} is the Dzyaloshinskii–Moriya vector [19]. Our results suggest that under DMI conditions, (a) the zone of positive H_{off} in pillar MTJs was enlarged under MTJ shrinkage; (b) H_{off} distribution in the 20 nm step MTJ was closer to that in a 80 nm pillar MTJ. In general, these results are consistent with that obtained in figure 5. Thus, we propose that step structure is superior to pillar structure, in terms of resistance to the H_{off} increase and switching asymmetry induced by MTJ shrinkage.

An important parameter that confirms data retention is the Δ because it is proportional to MTJ volume and decreases as the MTJ is scaled down. Thus, we finally calculated Δ for AP $\rightarrow$ P/P $\rightarrow$ AP switching to provide a different view on the effect of dimensional change on the pillar and step MTJs. Note that the (average) H_{stray} effect was included in the two structures for Δ calculations. In figure 7(a), we present Δ versus applied field for AP $\rightarrow$ P/P $\rightarrow$ AP for a 100 nm MTJ, and an intersection (defined as H_{switch} henceforth) at $\sim$140 Oe was obtained. This means that when given $H_{switch} = 140$ Oe, AP $\rightarrow$ P and P $\rightarrow$ AP would share the same switching energy

barrier. The smaller the H_{switch}, the closer the AP $\rightarrow$ P and P $\rightarrow$ AP are to the same in terms of switching. Again, due to the fact that 100 nm was the first data point in calculation, the two structures were forced to share the same H_{switch} in figure 7(a). We then reduced the dimension to 30 nm, as shown in figure 7(b), and significant difference was obtained in the two structures, in which the H_{switch} of the pillar MTJ increased significantly over 300 Oe (without considering the sidewall damage effect) but the H_{switch} of the step MTJ remained around $\sim$120 Oe. We then took experimental Δ versus applied field for AP $\rightarrow$ P/P $\rightarrow$ AP, for the 30 nm pillar and step MTJs, as presented in figure 7(c). The data show that the experimental H_{switch} was close to that of the theoretical H_{switch} in the step MTJ, while the H_{switch} of the pillar MTJ dropped to $\sim$130 Oe. This value is much smaller than that obtained in the theoretical case in which the etching damage was not implemented in the model of the pillar MTJ. In figure 7(d) we added the etching sidewall effect to the pillar MTJ. We used the same parameters as figure 5, i.e. assuming that the sidewall damage caused an 2 nm area damage on the CoFeB FL, resulting in a 50%
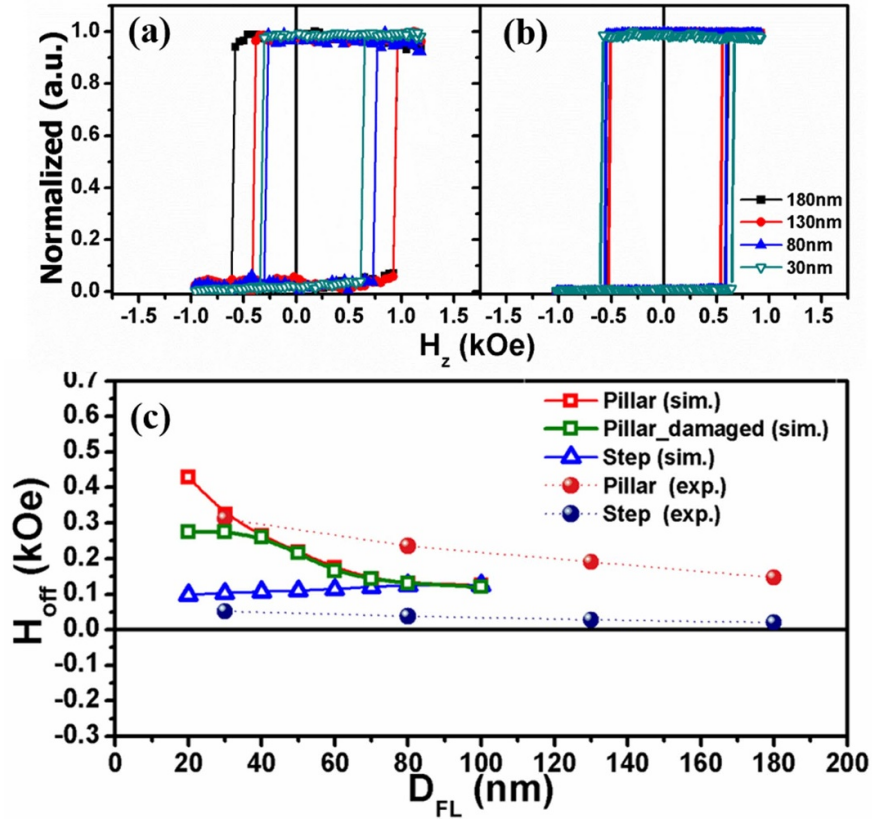
Figure 5. Normalized R-H loops of (a) pillar and (b) step MTJs with varying size. (c) H_{off} versus free-layer diameter obtained from experiments (filled symbols) and calculations (open symbols) for pillar and step MTJs. H_{off} obtained from the pillar MTJ in consideration of the sidewall damage effect (green open symbols) was also calculated for comparison.
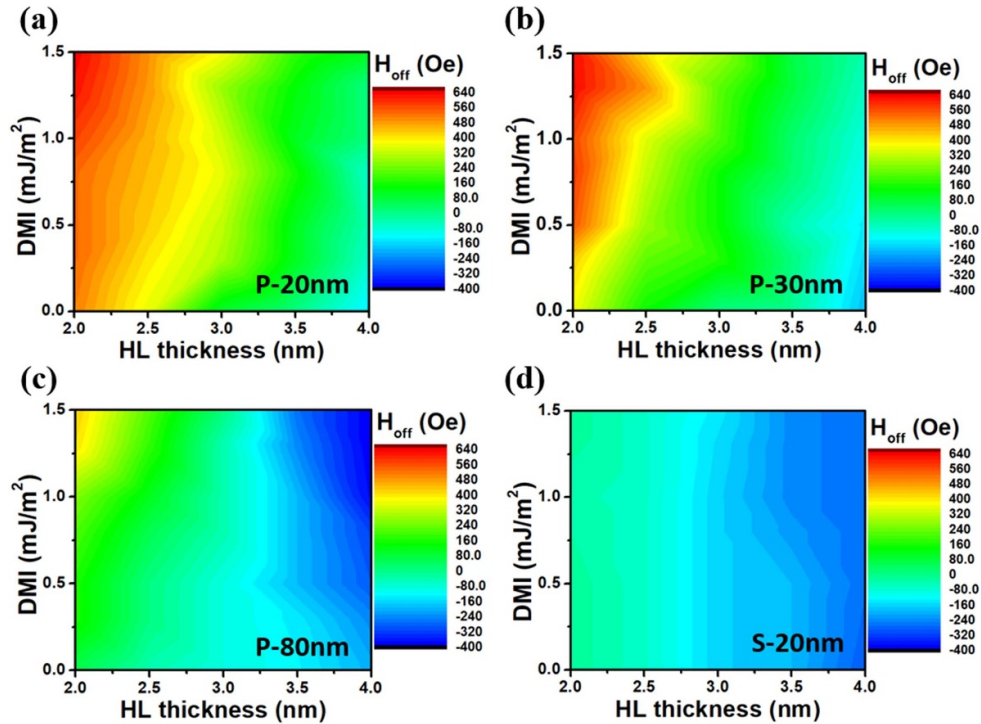

Figure 6. H_{off} contour maps of (a) 20 nm; (b) 30 nm; and (c) 80 nm pillar and (d) 20 nm step MTJs plotted as a function of DMI strength (0–1.5 mJ m^{-2}) and HL thickness (2.0–4.0 nm).
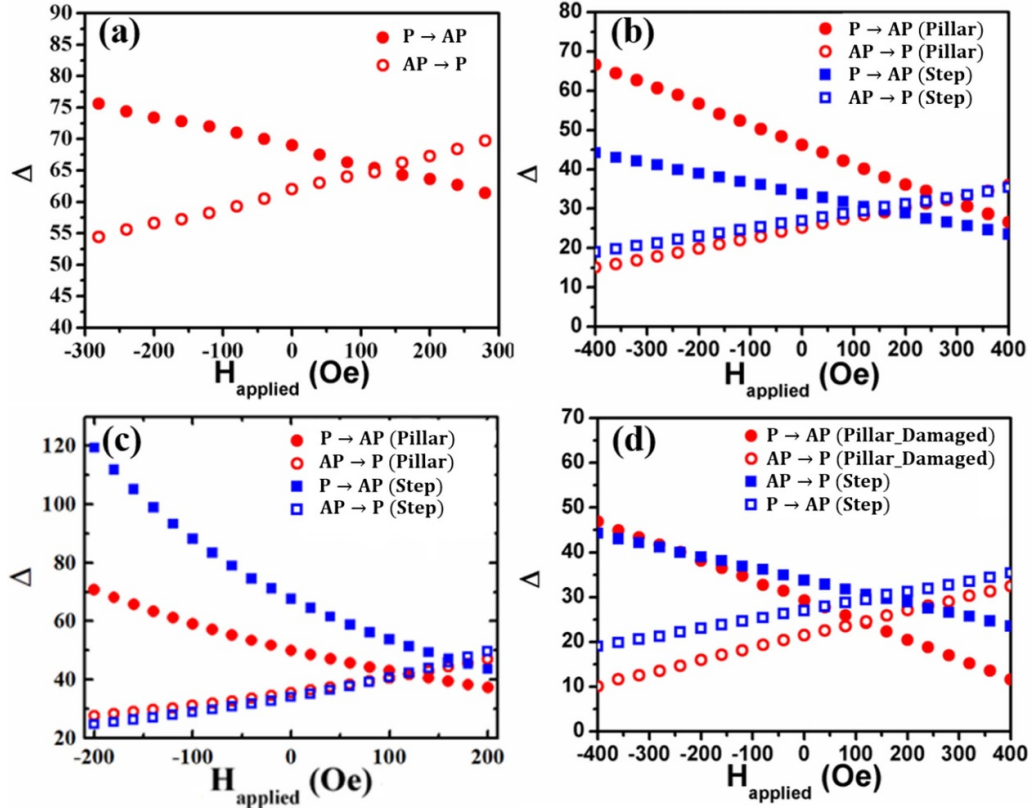
Figure 7. Thermal stability (Δ) calculations for AP$\rightarrow$P/P$\rightarrow$AP switching for (a) a 100 nm MTJ and (b) a 30 nm MTJ with pillar and step structures. (c) experimentally extracted Δ and (d) calculated Δ for the 30 nm pillar and step MTJs with AP$\rightarrow$P/P$\rightarrow$AP switching; note that in (d) the sidewall damage effect was considered in pillar MTJ (detail can be seen in supplementary information SF-2).

loss of both K_u and M_s. The results show that the sidewall-corrected model is closer to the experimental results in terms of the value and trend of Δ. It is worthy to mention that the actual step MTJ [10, 26] is sharing a large SAF substrate underneath, and its sidewall damage is smaller than the theoretical (etching through bottom layer) expectation. To make the difference obvious in the 30 nm MTJ, we only added the sidewall damage effect to the pillar MTJ in figure 7(d). Interestingly, we found that by theory, the pillar MTJ appeared to have a larger H_{switch} than the step MTJ, but in a real case, it became opposite likely due to the sidewall damage effect. This is a trade-off that has to be noted in the process of MTJ miniaturization.

4. Conclusion

In summary, miniaturization is an important issue in MRAM technology. However, the MRAM stacking is very complex and it is too expensive for the industry to obtain the success of the fabrication until the final device is made. Thus, using theoretical simulations to predict the possible impacts of critical processes on the MTJ allows for the most economical planning of the MTJ design. In the current study, micromagnetic simulation was used to analyze the impacts of H_{stray}, sidewall damage and DMI on macroscopic H_{off} and Δ when applied to two mainstream etching schemes. Our objective is to develop a fundamental model that can predict reliability failures in MTJ miniaturization. Overall, the trends observed in simulations were consistent with those obtained in experiments. We also proved that the SAF structure can be adjusted to optimize H_{stray} and reduce variability in switching. The results above may provide certain guidance to the implementation of high-density STT-MRAM.

Data availability statement

All data that support the findings of this study are included within the article and supplementary material.

The data that support the findings of this study are available upon reasonable request from the authors.

Acknowledgments

ORCID iDs

Chih-I Wu ⓘ https://orcid.org/0000-0002-0404-6781
Yuan-Chieh Tseng ⓘ https://orcid.org/0000-0001-5258-6152

References

[1] Ikeda S, Hayakawa J, Lee Y M, Matsukura F, Ohno Y, Hanyu T and Ohno H 2007 Magnetic tunnel junctions for spintronic memories and beyond *IEEE Trans. Electron Devices* **54** 991

[2] Worledge D C, Hu G, Abraham D W, Sun J Z, Trouilloud P L, Nowak J, Brown S, Gaidis M C, O'Sullivan J and Robertazzi R P 2011 Spin torque switching of perpendicular Ta|CoFeB|MgO-based magnetic tunnel junctions *Appl. Phys. Lett.* **98** 022501

[3] Ikeda S, Miura K, Yamamoto H, Mizunuma K, Gan H D, Endo M, Kanai S, Hayakawa J, Matsukura F and Ohno H 2010 A perpendicular-anisotropy CoFeB–MgO magnetic tunnel junction *Nat. Mater.* **9** 721

[4] Kan J J *et al* 2016 Systematic validation of 2x nm diameter perpendicular MTJ arrays and MgO barrier for sub-10 nm embedded STT-MRAM with practically unlimited endurance *Proc. IEEE International Electron Devices Meeting* pp 27.4.1–4

[5] Bandiera S, Sousa R C, Dahmane Y, Ducruet C, Portemont C, Baltz V, Auffret S, Prejbeanu I L and Dieny B 2010 Comparison of synthetic antiferromagnets and hard ferromagnets as reference layer in magnetic tunnel junctions with perpendicular magnetic anisotropy *IEEE Magn. Lett.* **1** 3000204

[6] Devolder T, Carpenter R, Rao S, Kim W, Couet S, Swerts J and Kar G S 2019 Offset fields in perpendicularly magnetized tunnel junctions *J. Phys. D: Appl. Phys.* **52** 274001

[7] Gajek M *et al* 2012 Spin torque switching of 20 nm magnetic tunnel junctions with perpendicular anisotropy *Appl. Phys. Lett.* **100** 132408

[8] Wang Y H, Huang S H, Wang D Y, Shen K H, Chien C W, Kuo K M, Yang S Y and Deng D L 2012 Impact of stray field on the switching properties of perpendicular MTJ for scaled MRAM *2012 Int. Electron Devices Meeting* pp 29.2.1–4

[9] Chien C W *et al* 2014 Scaling properties of step-etch perpendicular magnetic tunnel junction with dual-CoFeB/MgO *IEEE Electron Device Lett.* **35** 738–40

[10] Igarashi J, Llandro J, Sato H, Matsukura F and Ohno H 2017 Magnetic-field-angle dependence of coercivity in CoFeB/MgO magnetic tunnel junctions with perpendicular easy axis *Appl. Phys. Lett.* **111** 132407

[11] Chen K M, Cheng C W, Wei J H, Hsin Y C and Tseng Y C 2020 Effects of synthetic antiferromagnetic coupling on back-hopping of spin-transfer torque devices *Appl. Phys. Lett.* **117** 072405

[12] Park H, Teramoto A, Tsuchimoto J, Hashimoto K, Suwa T, Hayashi M, Kuroda R, Tsunekawa K and Sugawa S 2019 Impact of CoFeB surface roughness on reliability of MgO films in CoFeB/MgO/CoFeB magnetic tunnel junction *Japan. J. Appl. Phys.* **58** SIIB29

[13] Yoshida C, Tanaka T, Ataka T and Furuya A 2018 Micromagnetic study of probabilistic switching behavior in sub 20 nm-CoFeB/MgO magnetic tunnel junction *Non-Volatile Memory Technology Symp.* pp 1–5

[14] Huang J, Sim C H, Naik V B, Tran M, Ter Lim S and Han G 2015 Effect of the stray field profile on the switching characteristics of the free layer in a perpendicular magnetic tunnel junction *J. Appl. Phys.* **117** 17B721

[15] Lavanant M, Vallobra P, Watelot S P, Lomakin V, Kent A D, Sun J and Mangin S 2019 Asymmetric magnetization switching in perpendicular magnetic tunnel junctions: role of the synthetic antiferromagnet's fringe field *Phys. Rev. Appl.* **11** 034058

[16] Donahue M J 1999 *OOMMF User's Guide, Version 1.0* (Gaithersburg: US Department of Commerce, National Institute of Standards and Technology) p 6376

[17] Dzialoshinskii I E 1957 Thermodynamic theory of weak ferromagnetism in antiferromagnetic substances *Sov. Phys - JETP* **5** 1259

[18] Moriya T 1960 Anisotropic superexchange interaction and weak ferromagnetism *Phys. Rev.* **120** 91

[19] Fert A and Levy P M 1980 Role of anisotropic exchange interactions in determining the properties of spin-glasses *Phys. Rev. Lett.* **44** 1538

[20] Jang P H, Song K, Lee S J, Lee S W and Lee K J 2015 Detrimental effect of interfacial Dzyaloshinskii–Moriya interaction on perpendicular spin-transfer-torque magnetic random access memory *Appl. Phys. Lett.* **107** 202401

[21] Sampaio J, Khvalkovskiy A V, Kuteifan M, Cubukcu M, Apalkov D, Lomakin V, Cros V and Reyren N 2016 Disruptive effect of Dzyaloshinskii–Moriya interaction on the magnetic memory cell performance *Appl. Phys. Lett.* **108** 112403

[22] Thomas L *et al* 2014 Perpendicular spin transfer torque magnetic random access memories with high spin torque efficiency and thermal stability for embedded applications (invited) *J. Appl. Phys.* **115** 172615

[23] Bouquin P, Rao S, Kar G S and Devolder T 2018 Size dependence of spin-torque switching in perpendicular magnetic tunnel junctions *Appl. Phys. Lett.* **113** 222408

[24] Chaves-O'Flynn G D, Wolf G, Sun J Z and Kent A D 2015 Thermal stability of magnetic states in circular thin-film nanomagnets with large perpendicular magnetic anisotropy *Phys. Rev. Appl.* **4** 024010

[25] Sato H, Enobio E C I, Yamanouchi M, Ikeda S, Fukami S, Kanai S, Matsukura F and Ohno H 2014 Properties of magnetic tunnel junctions with a MgO/CoFeB/Ta/CoFeB/MgO recording structure down to junction diameter of 11 nm *Appl. Phys. Lett.* **105** 062403

[26] Shinozaki M, Dohi T, Igarashi J, Llandro J, Fukami S, Sato H and Ohno H 2020 Probing edge condition of nanoscale CoFeB/MgO magnetic tunnel junctions by spin-wave resonance *Appl. Phys. Lett.* **117** 202404